Density functional study of condensation in capped capillaries

P Yatsyshin[1] and N Savva[2,1] and S Kalliadasis[1]

[1] Department of Chemical Engineering, Imperial College London, London SW7 2AZ, United Kingdom

[2] School of Mathematics, Cardiff University, Cardiff, CF24 4AG, United Kingdom

Abstract. We study liquid adsorption in narrow rectangular capped capillaries formed by capping two parallel planar walls (a slit pore) with a third wall orthogonal to the two planar walls. The most important transition in confined fluids is arguably condensation, where the pore becomes filled with the liquid phase which is metastable in the bulk. Depending on the temperature T, the condensation in capped capillaries can be first-order (at $T \leq T_{\text{cw}}$) or continuous (at $T > T_{\text{cw}}$), where T_{cw} is the capillary wetting temperature. At $T > T_{\text{cw}}$, the capping wall can adsorb mesoscopic amounts of metastable under-condensed liquid. The onset of condensation is then manifested by the continuous unbinding of the interface between the liquid adsorbed on the capping wall and the gas filling the rest of the capillary volume. In wide capped capillaries there may be a remnant of wedge filling transition, which is manifested by the adsorption of liquid drops in the corners. Our classical statistical mechanical treatment predicts a possibility of three-phase coexistence between gas, corner drops and liquid slabs adsorbed on the capping wall. In sufficiently wide capillaries we find that thick prewetting films of finite length may be nucleated at the capping wall below the boundary of the prewetting transition. Prewetting then proceeds in a continuous manner manifested by the unbinding interface between the thick and thin films adsorbed on the side walls. Our analysis is based on a detailed numerical investigation of the density functional theory for the fluid equilibria for a number of illustrative case studies.

PACS numbers: 31.15.-p, 05.20.Jj, 68.08.Bc, 68.18.Jk

Submitted to: *J. Phys.: Condens. Matter*

1. Introduction

Applications of adsorption in confined geometries range from the latest developments in micro- and nanofluidics, the design of surfaces with controllable wetting properties [1–4], to colloidal science and bioengineering [5–7]. At the same time, the rich surface phase behavior of confined fluids, which arise when the parameters of the substrate geometry and the fluid-substrate intermolecular potential act as thermodynamic variables [8–10] makes their study particularly attractive from the fundamental point of view. When fluids are confined in nano-pores, where the characteristic dimensions exceed the ranges of molecular interactions by only one or two orders of magnitude, a satisfactory theoretical description has to account for the inhomogeneities of the fluid structure and the non-local character of molecular interactions. The density functional theory (DFT) for fluids meets these requirements by offering a classical framework which introduces the spatial dependence of the fluid density in the equation of state by approximating the free energy of the fluid as a functional of the one-body fluid number density. Reasonably far from critical points, the results of DFT are rather robust in describing the interfacial properties and structure of soft systems [11–14]. One can obtain interfaces, menisci shapes, and even complete surface phase diagrams with the single systematic approach offered by DFT, which is also significantly less expensive computationally compared to molecular dynamics simulations [15, 16]. Although classical DFT approaches were originally developed to study systems at equilibrium, recent progress in the area also includes the extension to dynamic DFTs which account for various hydrodynamic effects [17, 18].

Consider a capped capillary pore sketched in figure 1. It is translationally invariant along the z-axis, has macroscopic length along x-axis, and its width H along the y-axis is of the order of several tens of molecular diameters. The pore is filled with a Lennard-Jones (LJ) fluid at temperature T and chemical potential $\mu < \mu_{\rm sat}(T)$, where $\mu_{\rm sat}$ is the bulk saturation value. Far from the capping wall, as $x \to \infty$, the fluid density across the capillary is essentially the same as the density of the fluid across a slit pore of the same width (the associated slit pore). In the slit pore, a liquid-like phase metastable in the bulk (capillary liquid) can coexist with gas (capillary vapor) during condensation at $\mu_{\rm c} < \mu_{\rm sat}$ [19, 20]. Within the macroscopic Kelvin approximation, the condensation value is given by

$$\mu_{\rm c} = \mu_{\rm sat} - \frac{2\gamma_{\rm vl}\cos\Theta}{H\left(\rho_{\rm liq} - \rho_{\rm vap}\right)}, \tag{1}$$

where $\gamma_{\rm vl}$ is the vapor-liquid surface tension, Θ is Young's contact angle, $\rho_{\rm vap}$ and $\rho_{\rm liq}$ are the densities of the saturated vapor and liquid. In the capped capillary the cumulative attractive effect of the slab of substrate behind the capping wall may lead to the nucleation of capillary liquid on its surface even at $\mu < \mu_{\rm c}$. In this case, capillary liquid is metastable in the associated slit pore, so the phase adsorbed forms a slab of finite length. The mechanism is analogous to the adsorption of liquid film on a planar wall immersed in gas [19, 21]. By analogy with wall wetting, it is natural to

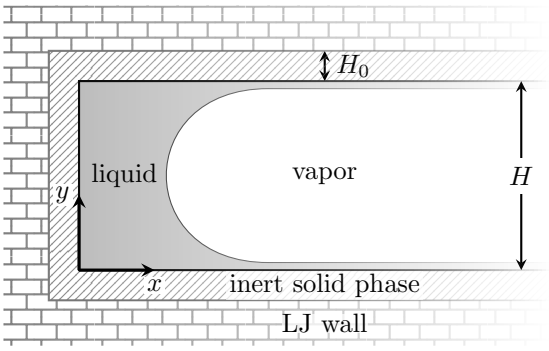

Figure 1. Capped capillary of width H opening into a reservoir filled with gas at temperature T and chemical potential $\mu < \mu_{\text{sat}}$. The system is transnationally invariant along the z-axis (orthogonal to the page). The bricked area is a LJ substrate. The hatched area is an inert wall coating of width H_0. The grey-shaded area shows the capillary liquid adsorbed from the gas.

expect that condensation in capped capillaries may be first-order or continuous. The existence of continuous condensation transition has first been put forward by Parry *et al.* [22], whereas a subsequent investigation by the present authors [23] demonstrated the existence of the capillary wetting temperature T_{cw}, such that at $T \leq T_{\text{cw}}$ condensation is first-order and at $T \leq T_{\text{cw}}$, condensation is continuous. In another theoretical and experimental study, Rascon *et al.* explored the nature of transition at T_{cw} and revealed a relation between T_{cw} and Young's contact angle of the capping wall, by approximating the complicated fluid-fluid and fluid-substrate interactions by a local effective Hamiltonian [24]. By accounting for the non-localities of molecular interactions captured through DFT, the present authors recently showed that the approximation found by Rascon *et al.* that the capillary wetting temperature is roughly equal to the planar wetting temperature of the capping wall is reasonable for sufficiently wide capillaries [25]. Noteworthy also are a number of works by other authors investigating capped capillaries from different perspectives. Darbellay and Yeomans studied saturated fluid in contact with a groove-like substrate and showed that condensation in grooves is continuous, unlike condensation in slit pores [26]. Roth and Parry investigated drying in over-saturated square-well fluid confined in a capped capillary, and found that capillary evaporation can also be continuous [27]. Lastly, Malijevsky investigated wetting in the same geometry and reported hysteresis in adsorption isotherms of fluids with short-range fluid-fluid interactions [28].

In the present work we substantially extend our earlier analysis [23]. We consider a number of examples which demonstrate the richness of the fluid phase behavior and are suggestive of the general features of wetting in nano-sized capped capillaries. For example, we explore in detail the connections in wetting of capped capillaries and wedge-shaped pores, since the capped capillary shown in figure 1 can be viewed as a right-angled wedge near the origin and as $H \to \infty$ [29]. Moreover, we find that the formation of prewetting films, which occurs for sufficiently large H and for $\tilde{\mu}_{\text{pw}} < \mu_{\text{c}}$, where $\tilde{\mu}_{\text{pw}}$

corresponds to the shifted prewetting of the walls of a slit pore of width H [30], is a continuous transition in capped capillaries, as opposed to the associated slit pores in which the transition is first order [19]. This difference can be attributed to the interaction of the fluid with the capping wall, which, as we will see, is responsible for a strikingly different physics of capped capillary when compared to slit pores.

The behavior of fluids in nano-pores is determined by the complicated interplay between molecular fluid-fluid and fluid-substrate interactions. Unravelling the various wetting mechanisms can only be achieved through a detailed computation or a carefully set up experiment. Here, we perform a parametric study of the DFT model of adsorption for a number of illustrative case studies. Most of the technical complexity of the approach can be encapsulated within our numerical methodologies [31], as they provide the means to obtain the phase portrait of the system in a systematic manner. This allows us to argue in terms of the fluid structure and its phenomenology, and elucidate the connections between wetting of different systems. In order to construct a roadmap of the possible scenarios, the case studies we present are of increasing complexity, considering their isotherms and full wetting phase diagrams. It is important to emphasize, however, that in the present work we neglect the fluctuations of the fluid density along the z-axis (see figure 1). Including fluctuations requires a non-classical approach, and is of separate interest [24]. In the following section we provide details of the DFT approximation employed, section 3 contains the discussion of phenomenology revealed by our numerical experiments, which is summarized in the concluding remarks of section 4.

2. Density functional and governing equations

The fluid-fluid and fluid-substrate molecular interactions are given by the LJ potential:

$$\varphi_{\varepsilon,\sigma}^{6-12}(r) = 4\varepsilon\left[-\left(\frac{\sigma}{r}\right)^{6} + \left(\frac{\sigma}{r}\right)^{12}\right], \tag{2}$$

where ε and σ control the well depth and the range of the potential, respectively. Treating the substrate as a spectator phase, we can obtain the cumulative potential $V(\mathbf{r})$ acting on a fluid molecule located at $\mathbf{r}$

$$V(\mathbf{r}) = \rho_0 \int_v \mathrm{d}\mathbf{r}' \varphi_{\varepsilon_0,\sigma_0}^{6-12}(|\mathbf{r}-\mathbf{r}'|), \tag{3}$$

i.e. it is given as an integral over the volume v occupied by the substrate, with ρ_0 being the effective density of the substrate material. The expression above exhibits a non-physical divergence at contact with the fluid. As a result, the fluid density decays super-exponentially at contact with the substrate walls [31]. Capturing this behaviour of the fluid density numerically requires a lot of mesh points near the wall, which unnecessarily increases the computational cost, given that the present study is focused on liquid–gas interfaces. We have therefore chosen to introduce a parameter H_0 as a means to remove some of the fluid layering near the wall by regularizing the behaviour of $V(\mathbf{r})$ at the fluid–wall interface. This essentially corresponds to introducing

a coating of the substrate walls with a layer of some foreign inert material of width H_0. The coating serves to remove the singularity of $V(\mathbf{r})$ at contact, because the LJ wall is then situated at distance H_0 from the fluid–substrate border. By doing so, the volume v over which the integral in (3) is computed excludes the volume occupied by the foreign material (see hatched area in figure 1). The foreign material coating the wall is such that it does not exert any long-range forces on the fluid, and thus does not change the physics of wetting: at high temperatures (above the bulk triple point) the physics of wetting by liquid is controlled by the asymptotic tails of the interaction potentials [33]. For example, it is straightforward to show that the value of planar Hamaker constant [33] is not affected by a finite shift H_0 of the planar wall potential [25]. Employing a shifting parameter H_0 is reasonable also because the molecular interactions at close distances are known not to be well described by the LJ potential, and in fact the substrate potentials obtained using *ab initio* quantum mechanics have a shifting parameter similar to H_0 [32].

Referring to the capped capillary sketched in figure 1, the fluid occupies the domain $[0,\infty]\times[0,H]\times[-\infty,\infty]$ along x-, y- and z-axes, respectively, and (3) takes the form:

$$V_{\mathrm{cpd}}(x,y)=\rho_0\int_{-\infty}^{\infty}\mathrm{d}z'\times\left(\int_{-\infty}^{\infty}\mathrm{d}x'\times\left(\int_{-\infty}^{-H_0}\mathrm{d}y'+\int_{H+H_0}^{+\infty}\mathrm{d}y'\right)+\int_{-\infty}^{-H_0}\mathrm{d}x'\int_{-H_0}^{H+H_0}\mathrm{d}y'\right)\times\varphi^{6\text{-}12}_{\varepsilon_0,\sigma_0}\left(\sqrt{(x-x')^2+(y-y')^2+z'^2}\right). \tag{4}$$

We also consider the limiting cases of (4), which correspond to the potentials of the planar wall (the fluid occupies the volume $[-\infty,\infty]\times[0,\infty]\times[-\infty,\infty]$):

$$V_{\mathrm{wll}}(y)\equiv\lim_{H\to\infty}\lim_{x\to\infty}V_{\mathrm{cpd}}(x,y), \tag{5}$$

the slit pore (the fluid occupies the volume $[-\infty,\infty]\times[0,H]\times[-\infty,\infty]$)

$$V_{\mathrm{slt}}(y)\equiv\lim_{x\to\infty}V_{\mathrm{cpd}}(x,y), \tag{6}$$

and the right-angled wedge (the fluid occupies the volume $[0,\infty]\times[0,\infty]\times[-\infty,\infty]$)

$$V_{\mathrm{wdg}}(x,y)\equiv\lim_{H\to\infty}V_{\mathrm{cpd}}(x,y). \tag{7}$$

2.1. Grand free energy functional

In broad terms, with DFT we construct approximations for the free energy functional of the fluid in contact with the substrate, by taking as input the model of molecular fluid-fluid and fluid-substrate interactions. More sophisticated DFTs may even reproduce experimental results, consider, e.g., the recent studies of adsorption of Argon, Neon and Xenon on planar substrates of various compositions [34–37]. A systematic development of the formalism can be found, e.g., in topical reviews [12–14, 16, 38]. The grand free energy functional of the fluid in contact with the substrate is given by

$$\Omega[\rho(\mathbf{r})]=F_{\mathrm{in}}[\rho(\mathbf{r})]+\int\mathrm{d}\mathbf{r}\rho(\mathbf{r})(V(\mathbf{r})-\mu), \tag{8}$$

where integration is carried out over the domain occupied by the fluid and $F_{\mathrm{in}}[\rho]$ is the intrinsic fluid free energy functional, which does not depend on the external potential

$V(\mathbf{r})$. The equilibrium density distribution $\rho(\mathbf{r})$ minimizes $\Omega[\rho(\mathbf{r})]$, which is then equal to the grand potential $\Omega(\mu, T)$. We approximate $F_{\text{in}}[\rho]$ as a sum of the hard sphere fluid free energy, $F_{\text{hs}}[\rho]$, and a contribution due to attractions. The random phase approximation is used for the latter, which recovers the correct asymptote of the direct pair correlation function in the uniform limit [38]:

$$F_{\text{in}}[\rho(\mathbf{r})] = \int \mathrm{d}\mathbf{r} f_{\text{id}}(\rho(\mathbf{r})) + F_{\text{hs}}[\rho(\mathbf{r})] + \frac{1}{2}\int \mathrm{d}\mathbf{r} \int \mathrm{d}\mathbf{r}' \rho(\mathbf{r}) \rho(\mathbf{r}') \varphi_{\text{attr}}(|\mathbf{r} - \mathbf{r}'|), \tag{9}$$

where $f_{\text{id}}(\rho) = k_{\text{B}}T\rho(\ln(\lambda^3\rho) - 1)$ is the ideal gas free energy, k_{B} and λ are the Boltzmann constant and the thermal wavelength, respectively. The fluid-fluid potential $\varphi_{\text{attr}}(r)$ is obtained from the LJ potential using the Barker–Henderson perturbation expansion [39]:

$$\varphi_{\text{attr}}(r) = \begin{cases} 0, & r \le \sigma \\ \varphi^{\text{6-12}}_{\varepsilon,\sigma}, & r > \sigma \end{cases}, \tag{10}$$

where σ is equal to the hard sphere diameter in $F_{\text{hs}}[\rho(\mathbf{r})]$.

The approximation for the configurational part of the hard sphere fluid free energy corresponds to the Carnahan-Starling equation of state [40]:

$$\psi(\rho) = k_{\text{B}}T\frac{\eta(4 - 3\eta)}{(1 - \eta)^2}, \quad \eta = \pi\sigma^3\rho/6. \tag{11}$$

Two different approximations for $F_{\text{hs}}[\rho]$ are employed here, which can be written in the following general form:

$$F_{\text{hs}}[\rho] = \int \mathrm{d}\mathbf{r} \rho(\mathbf{r}) \psi(\bar{\rho}(\mathbf{r})), \quad \bar{\rho}(\mathbf{r}) = \int \mathrm{d}\mathbf{r}' W(\mathbf{r} - \mathbf{r}') \rho(\mathbf{r}), \tag{12}$$

where integration is carried out over the volume occupied by the fluid. The weighting function $W(\mathbf{r})$ can be chosen to increase the accuracy of the corresponding approximation for the pair-correlation function of the hard sphere fluid. We use a local density approximation (LDA) [38] and a weighted density approximation (WDA) [41]:

$$W(\mathbf{r}) = \begin{cases} \dfrac{3}{4\pi\sigma^3}\ \Theta(\sigma - r) & \text{for WDA,} \\ \delta(\mathbf{r}) & \text{for LDA,} \end{cases} \tag{13}$$

where $\Theta(r)$ and $\delta(\mathbf{r})$ are, respectively, the step- and delta-functions. The LDA neglects molecular correlations due to excluded volume interactions, but nevertheless is often used as part of the perturbative treatment of $F_{\text{in}}[\rho(\mathbf{r})]$ in (9). The WDA is arguably a better choice as it was designed to capture the jump that occurs in the direct pair correlation function of a hard sphere fluid at a distance σ [41]. Using WDA in (9) accounts for the effects of excluded volume molecular interactions responsible for layering and freezing in fluids. As a result, the WDA fluid density profiles possess a proper oscillatory-like structure near the substrate walls. The most accurate description of hard-sphere fluids is given by the fundamental measure theory [42, 43], which uses three

weighting functions but it is computationally much more demanding. Since we are not after an accurate description of the physics near the walls, both LDA and WDA are deemed sufficient for describing the features of the phenomenology in qualitative terms.

2.2. Governing equations

We can obtain $\rho(\mathbf{r})$ from the extremum condition expressed by the Euler-Lagrange equation ($\delta\Omega[\rho]/\delta\rho = 0$):

$$k_{\mathrm{B}}T\ln\rho(\mathbf{r}) + \psi(\rho(\mathbf{r})) + \int \mathrm{d}\mathbf{r}'\rho(\mathbf{r}')\,\psi'_{\rho}(\bar{\rho}(\mathbf{r}'))\,W(\mathbf{r}-\mathbf{r}') + \int \mathrm{d}\mathbf{r}'\rho(\mathbf{r}')\,\varphi_{\mathrm{attr}}(|\mathbf{r}-\mathbf{r}'|) + V(\mathbf{r}) - \mu = 0, \tag{14}$$

where $\psi'(\rho)$ denotes the derivative of $\psi(\rho)$ with respect to ρ. For fixed T we can obtain a set of solutions, $\{\rho(\mathbf{r})\}_{\mu}$, to the above equation parametrized by μ. The grand potential $\Omega(\mu)$ is a concave function of μ [44], so the density profiles which satisfy (14) and correspond to stable (and metastable) fluid configurations, also correspond to concave branches of $\Omega[\{\rho(\mathbf{r})\}_{\mu}]$ as a function of μ. The stable configurations (unlike the metastable ones) also form the lower envelope of $\Omega[\{\rho(\mathbf{r})\}_{\mu}]$ as a function of μ. The stable configurations from the set $\{\rho(\mathbf{r})\}_{\mu}$ may belong to different fluid phases, which can coexist at some value of μ, where $\Omega(\mu)$ is non-analytic. First-order and continuous phase transitions are characterized by jump discontinuities and singularities in the derivative of $\Omega(\mu)$, respectively.

During a first-order phase transition, at least two different equilibrium density configurations, $\rho_1(\mathbf{r})$ and $\rho_2(\mathbf{r})$, satisfy the following

$$\frac{\delta\Omega}{\delta\rho}\Big|_{\rho_1(\mathbf{r})} = \frac{\delta\Omega}{\delta\rho}\Big|_{\rho_2(\mathbf{r})} = 0 \tag{15a}$$

$$\Omega[\rho_1(\mathbf{r})] - \Omega[\rho_2(\mathbf{r})] = 0. \tag{15b}$$

In the absence of walls [so that $V(\mathbf{r}) \equiv 0$], equations (15) provide the condition of saturation and are equivalent to the balance $\mu(\rho_{\mathrm{liq}}) = \mu(\rho_{\mathrm{vap}}) = \mu_{\mathrm{sat}}$ and $P(\rho_{\mathrm{liq}}) = P(\rho_{\mathrm{vap}}) = P_{\mathrm{sat}}$, where

$$\mu = k_{\mathrm{B}}T\ln\rho + \psi(\rho) + \rho\psi'_{\rho}(\rho) - \frac{32\pi}{9}\rho\sigma^3\varepsilon, \tag{16}$$

$$P = \rho k_{\mathrm{B}}T\frac{1+\eta+\eta^2-\eta^3}{(1-\eta)^3} - \frac{16\pi}{9}\rho^2\sigma^3\varepsilon. \tag{17}$$

The presence of walls may lead to surface phase coexistence [19]. In that case, it is often convenient to split the grand potential into the bulk and excess contributions. Usually the bulk parts are equal in both coexisting phases, but the excess parts are different [45].

We solve (14) and (15) numerically. Wetting of a planar wall and a slit pore are treated as one-dimensional (1D) numerical problems, whereas a capped capillary and a right-angled wedge as two-dimensional (2D) problems. The working expressions for the interaction potentials are provided in Appendix A. In practice, the domain is discretized

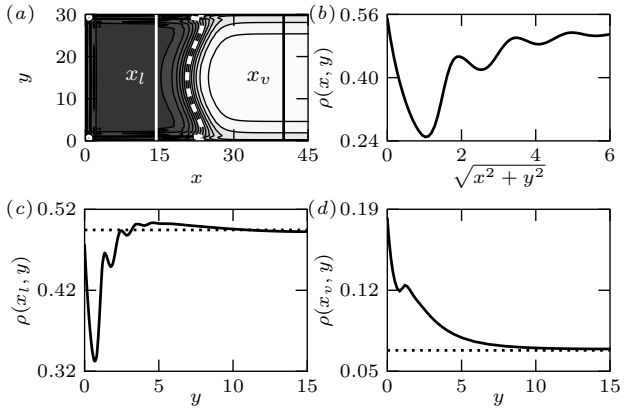

Figure 2. (a) Density profile for a capped capillary with $H = 30$, $\varepsilon_0 = 0.85$, $\sigma_0 = 1.5$, $H_0 = 2.8$ ($T_\mathrm{w} = 0.868$), at $T = 0.88$, $\Delta\mu = -2.4 \times 10^{-2}$; fluid treated in WDA. The vertical lines mark the position of slices inside the capillary liquid, at $x_\mathrm{l} = 14$, and inside the gas, at $x_\mathrm{g} = 40$. (b) Slice along the corner bisector. (c) and (d) Slices inside capillary liquid and gas at x_l and x_g (shown for $0 \le y \le H/2$); the dotted horizontal lines are drawn at $\rho^\mathrm{c}_\mathrm{liq} = 0.5$ and $\rho^\mathrm{c}_\mathrm{vap} = 0.07$ for (c) and (d), respectively.

on a tensor product grid, which extends the spectral collocation method detailed in our previous work [31] to 2D. Given the grid of conformally mapped Chebyshev collocation points, all functions (including the unknown density profiles), are represented by a unique polynomial [25], and integration is performed by computing matrix-vector products. Noteworthy is that the spectral collocation approach allows us to represent the fluid-fluid interaction potential (10) on the whole, untruncated, calculation domain. By discretising only the domain occupied by the fluid, the hard wall boundary condition, i.e. that the fluid density vanishes inside the substrate volume, is automatically satisfied. Equations (14) and (15) are then reduced to a system of non-linear algebraic equations, which we solve with Newton iterations. We use arc-length continuation technique (also detailed in our previous work [31]) to obtain families of solutions to equations (14) and (15) parametrized by μ and T. This allows us to obtain isotherms of wetting and phase coexistence curves of various transitions.

In order to verify the numerical implementation, we have performed convergence tests of the computer code developed to solve (14) in 2D with LDA and WDA for the hard sphere part of the functional, see Appendix B. We also verified that the exact Gibbs adsorption rule – see below – and the appropriate planar contact sum rules [25, 43] are satisfied by the density profiles we obtain. Additionally, we made sure that the density profiles of the planar wall and slit pore obtained using 1D and 2D solvers agree to within the tolerance of the Newton method, taken to be 10^{-6}. The fact that the planar wall wetting temperatures T_w obtained from the Euler-Lagrange equation (14) (by computing Young's contact angle), and from the coexistence condition (15) (by computing the wall prewetting curve) agree (see Appendix C) further attests to the correct implementation of the numerical code for solving (15).

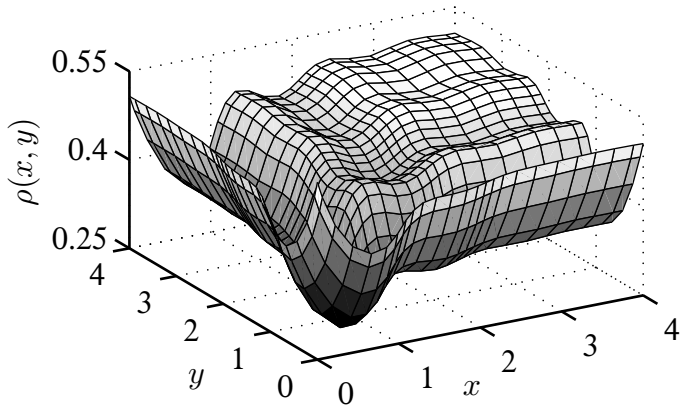

Figure 3. Surface plot of the density profile from figure 2(a). The near-apex oscillations and the near-wall layering are caused by the non-local excluded volume molecular interactions.

3. Wetting phenomenology

Throughout this work we choose the parameters σ and ε of the fluid-fluid potential (10) to be the units of length and energy in our computations. The bulk critical temperature is then $T_{\rm c} = 1.006$. It is also convenient to define $\Delta\mu = \mu - \mu_{\rm sat} < 0$, and plot isotherms and phase diagrams using $\Delta\mu$ instead of μ. The dimensionless expressions for the fluid-fluid and fluid-substrate potentials are provided in Appendix A. In our computations we fixed $\rho_0 = 1$ and varied the remaining substrate parameters, ε_0, σ_0 and H_0. In the present work we restrict our attention to combinations of ε_0, σ_0 and H_0, which give rise to first-order wetting in the planar wall case, as they typically exhibit a rich surface phase behavior [11,21,29]. Another criterion for the specific choices of ε_0, σ_0 and H_0 was to illustrate different possible wetting scenarios. In Appendix C we present the phase diagrams of planar wall wetting for the combinations of ε_0, σ_0 and H_0 considered here. The phase diagrams of wetting in slit pores and capped capillaries are also computed in every case. For computational efficiency we also tried to select substrate materials with high values of wetting temperatures, in order for the gas-liquid interfaces not to be very steep, which require less computational cost to be resolved than steeper ones.

In order to obtain the fluid density distribution $\rho(\mathbf{r}) \equiv \rho_{\rm cpd}(x,y)$ for the capped capillary from figure 1, we use (4) to write $V(\mathbf{r}) \equiv V_{\rm cpd}(x,y)$. From (6), we must require that $\rho_{\rm cpd}(x,y) \to \rho_{\rm slt}(y)$, as $x \to \infty$, i.e. as we move far from the capping wall. Moreover, since the cumulative potential of the semi-infinite substrate slab which plugs the slit pore to form the capped capillary is given by

$$\begin{aligned} V_{\rm cap}(x,y) &= \rho_0 \int_{-\infty}^{-H_0} {\rm d}x' \int_{-H_0}^{H+H_0} {\rm d}y' \int_{-\infty}^{\infty} {\rm d}z' \;\; \varphi^{6-12}_{\varepsilon_0,\sigma_0}(|\mathbf{r}-\mathbf{r}'|) \\ &= \frac{-3}{8}\frac{\rho_0\varepsilon_0\sigma_0^6\pi H}{x^4} + O\left(\frac{\rho_0\varepsilon_0\sigma_0^6 H H_0}{x^5}\right) \;\text{ as } x \to \infty, \end{aligned} \tag{18}$$

we find that $\rho_{\rm cpd}(x,y) = \rho_{\rm slt}(y) + O(x^{-4})$, as $x \to \infty$, where the next-order term can

be readily obtained from the asymptotics of (14), by following the same procedure used in [31] for a planar wall. So, in order to study the capped capillary, we need to obtain the fluid density $\rho_{\text{slt}}(y)$ for the associated slit pore for the values of μ and T of interest. Just like the capped capillary, the fluid density $\rho(\mathbf{r}) \equiv \rho_{\text{slt}}(y)$ is found from (14), using (6) to set $V(\mathbf{r}) \equiv V_{\text{slt}}(y)$. From the conditions of phase coexistence, (15), we can also obtain the condensation curve $\mu_{\text{c}}(T)$, which is sometimes approximated by the Kelvin equation, (1). Since according to (6) the potential of the slit pore is a limiting case of the potential of the capped capillary, $\mu_{\text{c}}(T)$ also corresponds to the locus of non-analyticities of the fluid free energy in the case of the capped capillary.

A typical density distribution $\rho_{\text{cpd}}(x, y)$ at $\mu \lesssim \mu_{\text{c}}$ is presented in figures 2 and 3. The data in the contour plot [figure 2(a)] is scaled between $\rho^{\text{c}}_{\text{vap}}$ (white) and $\rho^{\text{c}}_{\text{liq}}$ (dark grey), which are the roots of equation (16) at $\mu = \mu_{\text{c}}$. The fluid density has a distinct oscillatory behavior at contact with the substrate. Considering the slice along the corner bisector [figure 2(b)], we note pronounced oscillations set approximately one hard sphere diameter apart, which demonstrate the tight packing of molecular layers at the apex. Molecular layering at the corner and at the adjacent walls is better visualized in figure 3, where the local maxima of $\rho_{\text{cpd}}(x, y)$ correspond to the tight packing of individual fluid molecules. The amplitude of density oscillations rapidly decays into the volume of the fluid due to the increasing relative role of inter-molecular attractions. The same can be inferred from the vertical slice inside the capillary liquid (along x_{l}) shown in figure 2(c). Even along a slice at x_{g}, inside the gas, one can see a single near-wall oscillation [figure 2(d)]. The plateaus of near-constant values for $\rho(x_{\text{g}}, y)$ and $\rho(x_{\text{l}}, y)$ at $\rho^{\text{c}}_{\text{vap}}$ and $\rho^{\text{c}}_{\text{liq}}$, respectively, serve to show that the denser phase adsorbed on the capping wall is capillary liquid, which coexists with gas along a circular-arc meniscus. Structurally, the fluid phases on either side of the meniscus are essentially the same as the phases coexisting in a slit pore of the same width during capillary condensation. For wide pores, the fine near-wall details of the fluid density can be ignored, and one can approximately consider the slab to be of constant density $\rho^{\text{c}}_{\text{vap}}$.

3.1. Capillary wetting temperature and prewetting

We define the adsorption and the excess grand potential in the capped capillary relative to the associated slit pore:

$$\Gamma = \int_0^\infty \mathrm{d}x \int_0^H \mathrm{d}y \left[\rho_{\text{cpd}}(x, y) - \rho_{\text{slt}}(y)\right], \tag{19}$$

$$\Omega^{\text{ex}} = \Omega\left[\rho_{\text{cpd}}(x, y)\right] - \Omega\left[\rho_{\text{slt}}(y)\right], \tag{20}$$

where the first and second terms in (20) are given by (8) with $V \equiv V_{\text{cpd}}$ and $V \equiv V_{\text{slt}}$, respectively. We use Ω^{ex} because in the case of the capped capillary the computation of Ω from (8) involves integrating the grand free energy density over a domain unbounded along the x-axis, which does not yield a finite value. On the other hand, using Ω^{ex} allows us to remove the slit pore contribution to Ω so that the value we obtain is bounded.

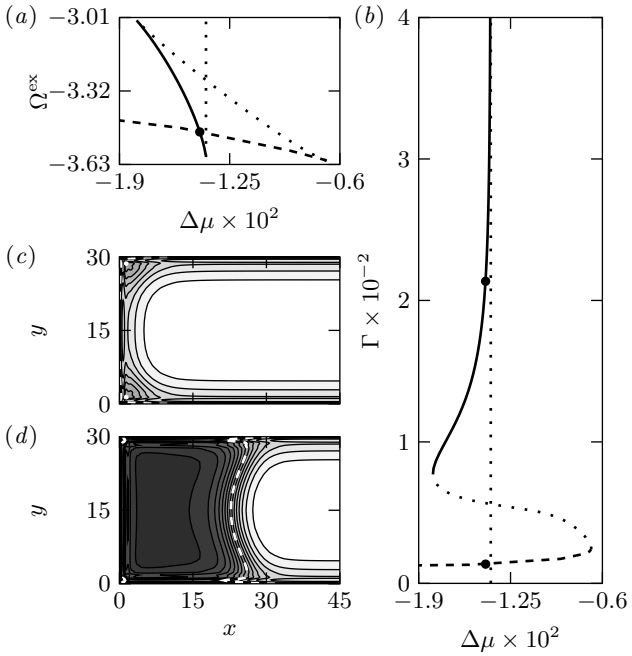

Figure 4. Capillary prewetting transition at $T = 0.93$, $\Delta\mu_{\rm cpw} = -1.43 \times 10^{-2}$ in the capillary with $H = 30$, $\varepsilon_0 = 0.85$, $\sigma_0 = 1.35$, $H_0 = 2.2$; fluid treated in WDA ($T_{\rm w} = 0.927$); $\Delta\mu_{\rm c} = -1.39 \times 10^{-2}$. (a) and (b) show adsorption and grand potential isotherms. Dashed, solid and dotted branches with spinodals at $\Delta\mu = -0.68 \times 10^{-2}$ and $\Delta\mu = -1.8 \times 10^{-2}$ correspond to gas, capillary liquid slabs, and unstable fluid states, respectively. Capillary prewetting at $\Omega^{\rm ex} = -3.49$ and $\Gamma = \{14, 214\}$ is marked by filled circles. Dotted vertical lines are drawn at $\Delta\mu_{\rm c}$. (c) and (d) show the density profiles at $\mu_{\rm cpw}$, shaded linearly between $\rho^{\rm c}_{\rm vap} = 0.1$ (white) and $\rho^{\rm c}_{\rm liq} = 0.43$ (dark grey).

Moreover, it is straightforward to show that the Gibbs adsorption rule takes the form $\Gamma = -R^{-1}\partial\Omega^{\rm ex}/\partial\mu$, where R is the macroscopic system size along the z-axis [25]. When there is a single fluid phase in the associated slit pore at the given μ, both $\Gamma(\mu)$ and $\Omega^{\rm ex}(\mu)$ are unique and finite for any fluid configuration compatible with the boundary condition $\rho_{\rm cpd}(x, y) \to \rho_{\rm slt}(y)$, as $x \to \infty$.

Figure 4 shows a wetting isotherm which corresponds to a family of density profiles $\{\rho(\mathbf{r})\}_\mu$ obtained as a function of μ at a fixed $T < T_{\rm c}(H)$ (the critical temperature of the associated slit pore), where μ spans the interval from below condensation to nearly $\mu_{\rm c}$. The excess grand potential [figure 4(a)] and its derivative [figure 4(b)] show how hysteresis during adsorption is controlled by the reservoir parameter μ. The inflection points linking the three branches of $\Omega^{\rm ex}(\mu)$ provide the spinodals of gas (dashed branch) and capillary liquid slabs (solid branch). The lower envelope of $\Omega^{\rm ex}(\mu)$ (locus of configurations with minimal $\Omega^{\rm ex}(\mu)$ at any given μ) consists of the stable parts of the two branches, and is non-analytic in its first derivative at $\mu = \mu_{\rm cpw}$, at which the adsorption $\Gamma(\mu)$ undergoes a finite jump between the values marked by filled circles in figures 4(a) and 4(b). Therefore, $\mu_{\rm cpw}$ corresponds to a first-order transition. The fluid configurations coexisting at $\mu_{\rm cpw}$ are shown in figures 4(c) and 4(d). The gas phase

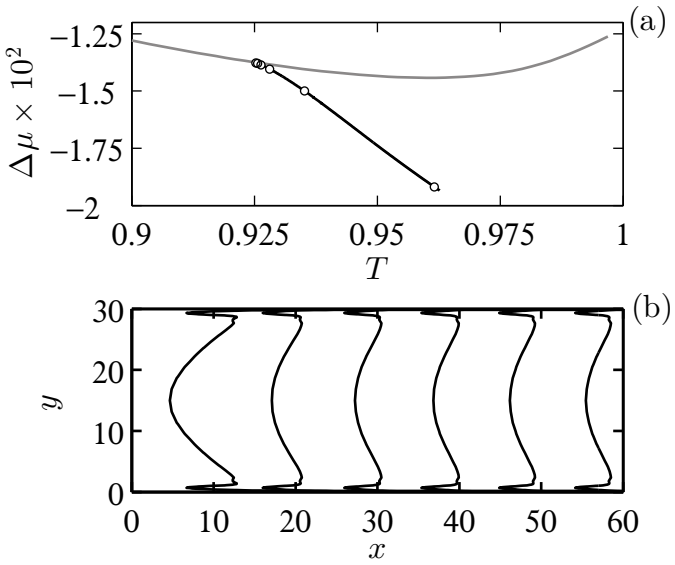

Figure 5. (a) Wetting phase diagram of the capped capillary from figure 4. Capillary prewetting, $\Delta\mu_{\rm cpw}(T)$ (black curve), approaches condensation, $\Delta\mu_{\rm c}(T)$ (grey curve), tangentially at $T_{\rm cw} = 0.925$. Open circles on $\Delta\mu_{\rm cpw}(T)$ correspond to the menisci of coexisting slab configurations plotted in (b). (b) The menisci correspond, left to right, to decreasing values of T: 0.9616, 0.9352, 0.9281, 0.9263, 0.9256, 0.9253.

extends from below $\mu_{\rm c}$, up to the right-hand spinodal. The slab phase extends from the left-hand spinodal, up to $\mu_{\rm c}$, where the length of the slab diverges. The divergence of $\Gamma(\mu)$ as $\mu \to \mu_{\rm c}$ is readily seen in the plot. Therefore, the nature of the non-analyticity of $\Omega(\mu)$ at $\mu_{\rm c}$ is a continuous phase transition. Due to (18), it is straightforward to deduce that

$$\Gamma(\mu) \propto (\mu_{\rm c} - \mu)^{-1/4}, \text{ as } \mu \to \mu_{\rm c}, \tag{21}$$

as also shown by Parry *et al.* using effective Hamiltonians [22].

Using (15), we can investigate capillary prewetting with temperature and obtain the $\mu_{\rm cpw}(T)$-curve [figure 5(a)], where capillary liquid slabs coexist with the gas pore at different temperatures. We find that the curves $\mu_{\rm cpw}(T)$ and $\mu_{\rm c}(T)$ appear to merge together at some temperature. When this happens, the menisci of the the coexisting slab configurations unbind from the capping wall with lowering T [figure 5(b)], and $\Gamma = \Gamma_{\rm slb}$ of the coexisting slab configurations diverges. We can argue theoretically that this is the case, by considering the surface Clausius-Clapeyron equation derived in Appendix D. Accordingly, for large $\Gamma_{\rm slb}$ we have

$$\frac{{\rm d}(\mu_{\rm c} - \mu_{\rm cpw})}{{\rm d}T} \propto \frac{1}{\Gamma_{\rm slb}}, \tag{22}$$

as $\Gamma_{\rm slb} \to \infty$, where the constant of proportionality is both temperature-dependent and positive. The above is equivalent to ${\rm d}\mu_{\rm c}/{\rm d}T \to {\rm d}\mu_{\rm cpw}/dT$ as $\Gamma_{\rm slb} \to \infty$, so $\mu_{\rm cpw}(T)$ approaches $\mu_{\rm c}(T)$ tangentially at the capillary wetting temperature, $T_{\rm cw}$. From the asymptotics of (21) and by integrating (22), we obtain

$$\mu_{\rm c} - \mu_{\rm cpw} \propto (T - T_{\rm cw})^{4/3} \tag{23}$$

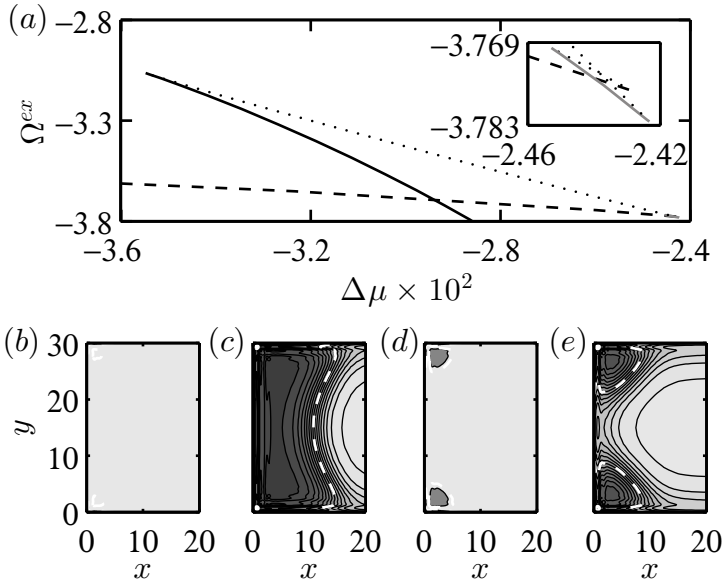

Figure 6. Capillary prewetting followed by a metastable transition to corner drops. (a) Excess grand potential isotherm of the capillary with parameters given in the caption of figure 2 at $T = 0.906$. The concave branches correspond to gas (dashed), capillary liquid slabs (solid black) and drops (solid grey, see inset). Dotted branches are unstable. Capillary prewetting at $\Delta\mu_{\rm cpw} = -2.94 \times 10^{-2}$ is stable [see profiles on (b) and (c)], the remnant of wedge prefilling at $\Delta\tilde{\mu}_{\rm wpf} = -2.44 \times 10^{-2}$ is metastable [see inset on (a) and profiles on (d) and (e)]. Note that the pairs of coexisting profiles (b), (c) and (d), (e) correspond in figure (a) to the intersection of the dashed branch with the solid black and grey branches, respectively.

as $T \to T_{\rm cw}$, which is valid for LJ intermolecular potentials. Equation (23) can be used to estimate the order of accuracy with which the value of $T_{\rm cw}$ is computed. Numerically, we cannot go to infinite $\Gamma_{\rm slb}$, and have to approximate $T_{\rm cw}$ with a value of $T \gtrsim T_{\rm cw}$ so that $\mu_{\rm cpw}(T) \lesssim \mu_{\rm c}(T)$. Thus, knowing the difference $\mu_{\rm c}(T) - \mu_{\rm cpw}(T)$, (23) can provide an estimate for $T - T_{\rm cw}$. In all the phase diagrams presented, we have been able to approach condensation to within $\mu_{\rm c} - \mu_{\rm cpw} = {\rm O}(10^{-3})$ along the capillary prewetting curve, which corresponds to an accuracy of ${\rm O}(10^{-4})$ within the quoted value of $T_{\rm cw}$. For $T < T_{\rm cw}$ capillary liquid slabs of finite lengths adsorbed on the capping wall are metastable. In general, for $\mu < \mu_{\rm c}$ the lower envelope of $\Omega^{\rm ex}(\mu)$ consists only of the gas branch, and condensation at $\mu_{\rm c}$ is first-order, just as in the associated slit pore. For $T > T_{\rm cw}$ the capping wall may nucleate capillary liquid for $\mu \geq \mu_{\rm cpw}(T)$. The length of adsorbed capillary liquid slab grows continuously with μ as $\mu \to \mu_{\rm c}$, and $\Gamma(\mu_{\rm c})$ is singular. The condensation is continuous and is manifested by the unbinding of the circular-arc meniscus of gas-capillary liquid interface.

3.2. Interplay with wedge wetting

By fixing the origin in figure 1 and taking the limit $H \to \infty$, the capped capillary becomes a wedge. Therefore, effects specific to wedge wetting should be manifested

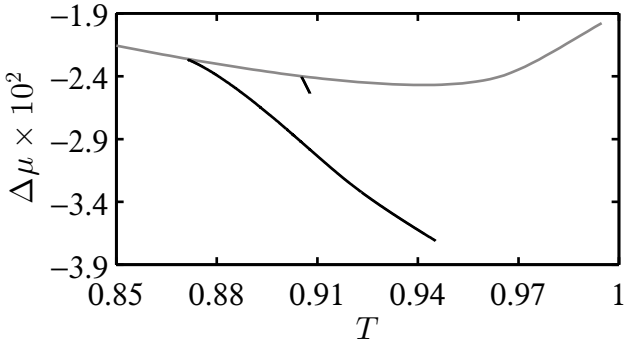

Figure 7. Wetting diagram of capillary from figures 2 and 6. Capillary prewetting (black) is tangential to condensation (grey) at $T_{\rm cw} = 0.871$, and pre-empts the remnant wedge prefilling, $\Delta\tilde{\mu}_{\rm wpf}(T)$ (black), which occurs approximately for $0.905 < T < 0.908$.

in capped capillaries with sufficiently isolated corners. Indeed, for a substrate already considered above (see figures 2 and 3), we find a transition between the gas and drop-like fluid configurations for a certain temperature range. Figure 6 shows an isotherm, where apart from capillary prewetting [see the intersection of dashed and solid black branches in figure 6(a) and the density profiles in figures 6(b) and 6(c)], we observe a transition to corner drops [see the intersection of solid grey and dashed branches magnified in the inset of figure 6(a) and the density profiles in figures 6(d) and 6(e)], which prompts a connection to wedge prefilling [29]. The transition to corner drops (remnant wedge prefilling) is metastable here, since the respective self-intersection of $\Omega^{\rm ex}(\mu)$ does not belong to the lower envelope of $\Omega^{\rm ex}(\mu)$. The wetting phase diagram in figure 7 shows that the remnant wedge prefilling is metastable everywhere and is pre-empted by capillary prewetting. We attribute such fluid behavior to the particularly small value of H, which leads to a significant Kelvin shift of the capillary coexistence curve $\mu_{\rm c}(T)$ with respect to its bulk counterpart $\mu_{\rm sat}(T)$. By increasing H the fluid confined in the pore behaves more like bulk fluid, i.e. the $\Delta\mu_{\rm c}(T)$-curve flattens and approaches $\Delta\mu \equiv 0$ [25]. At the same time, since the corners of the capped capillary become more isolated, the remnant wedge prefilling curve, $\Delta\tilde{\mu}_{\rm wpf}(T)$, spans a wider temperature range, uncovering a larger portion of the wedge prefilling curve, $\Delta\mu_{\rm wpf}(T)$. Given that $\Delta\mu_{\rm wpf}(T)$ is tangential to $\Delta\mu \equiv 0$ [29], for sufficiently wide capped capillaries there will be an intersection of $\Delta\tilde{\mu}_{\rm wpf}(T)$ and $\Delta\mu_{\rm cpw}(T)$, and corner drops can become stable. In what follows, we consider in some detail the DFT for prefilling transitions in wedges, which in turn allows us to discuss the general features of wetting in capped capillaries of different widths. More details on wedge wetting can be found, e.g. in the works by Hauge [46] and Rejmer *et al.* [29].

For a wedge with an opening angle 2α immersed in gas at $\Delta\mu \lesssim 0$, Hauge found that a macroscopic amount of liquid, which is metastable in the bulk, may coexist with undersaturated gas, if the former is situated on the concave side of the curved meniscus separating the two [46]. This condition is satisfied by a macroscopic amount

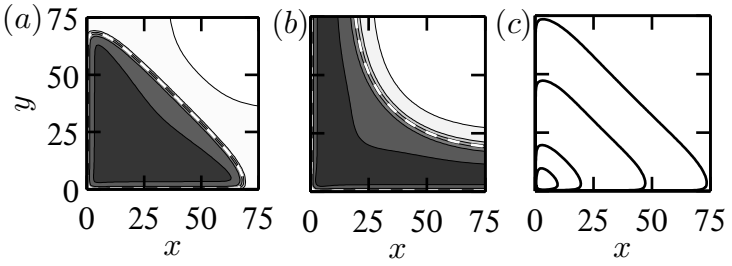

Figure 8. Wedge in undersaturated gas. Substrate parameters $\varepsilon_0 = 0.7$, $\sigma_0 = 2$, $H_0 = 5$; using LDA, $T_\mathrm{w} = 0.755$, $T_\mathrm{f} = 0.693$. (a) and (b) Stable configurations at $T_\mathrm{w} > T = 0.715 > T_\mathrm{f}$ ($\Theta = 36.3°$, $\rho_\mathrm{vap} = 0.02$, $\rho_\mathrm{liq} = 0.67$), $\Delta\mu = -1.5 \times 10^{-2}$ and $T = 0.89 > T_\mathrm{w}$ ($\Theta = 0$, $\rho_\mathrm{vap} = 0.08$, $\rho_\mathrm{liq} = 0.5$), $\Delta\mu = -0.8 \times 10^{-2}$, respectively. The data in the contour plots is scaled between the respective ρ_vap (white) and ρ_liq (dark grey), and the sharp interfaces are defined at $(\rho_\mathrm{vap} + \rho_\mathrm{liq})/2$. (c) Gas-liquid interfaces of configurations coexisting with gas during wedge prefilling. The interfaces, as we move outwards from the apex, correspond, respectively, to the following pairs of values of $\left(T, \Delta\mu \times 10^2\right)$: $(0.865, -5.8)$, $(0.8, -2.3)$, $(0.748, -0.6)$, $(0.73, -0.26)$.

of liquid adsorbed in the wedge apex if the temperature is higher than the wedge filling temperature T_f, for which $\Theta\left(T_\mathrm{f}\right) = \pi/2 - \alpha$, i.e. for a flat meniscus of zero curvature. Moreover, Hauge showed that the filling of the wedge by liquid is continuous for $T > T_\mathrm{f}$, and proceeds via the unbinding meniscus as $\Delta\mu \to 0$ isothermally. For $T > T_\mathrm{f}$ and $\Delta\mu < 0$ microscopic mean-field approaches predict first-order wedge prefilling transition [29], where a microscopic amount of liquid adsorbed in the apex coexists with gas. The locus of wedge prefilling, $\mu_\mathrm{wpf}\left(T\right)$, approaches saturation tangentially at T_f, and demarcates the region of stability of liquid drops adsorbed in the wedge apex.

Employing an LDA functional, which is less computationally expensive compared to other DFTs allowed us to perform a technically complicated parametric study in the T – $\Delta\mu$ space, in order to highlight the connections between wetting in a right-angled wedge and in rectangular capped capillaries of the same substrate material. In this case, $\alpha = \pi/4$ and we can obtain T_f by computing $\Theta\left(T\right)$ and solving $\Theta\left(T_\mathrm{f}\right) = \pi/4$ graphically (see Appendix C and figure C1 therein). The fluid density distribution inside the wedge, $\rho_\mathrm{wdg}\left(x, y\right)$, is found from (14) by using (7) to set $V\left(\mathbf{r}\right) \equiv V_\mathrm{wdg}\left(x, y\right)$ in (14). The curve $\mu_\mathrm{wpf}\left(T\right)$ is obtained using (15).

Computing the wedge prefilling curve in the vicinity of T_f is highly demanding and deserves a separate study. In the present work, we have restricted the temperature range for computing $\mu_\mathrm{wpf}\left(T\right)$ to $T \geq 0.735 > T_\mathrm{f} = 0.693$, see figures 9 (dotted curve) and 10 (curve 2, which – as expected – will approach the $\Delta\mu$ axis tangentially). Two stable fluid configurations at $\Delta\mu \lesssim 0$, and with the menisci at mesoscopic distances from the wedge apex are presented in figures 8(a) and 8(b), and correspond to temperatures below and above T_w, respectively. Figure 8(c) shows the interfaces of several drops coexisting with gas during the first-order transition along the $\mu_\mathrm{wpf}\left(T\right)$-curve. Note that as T approaches T_f, the amount of coexisting adsorbate grows, becoming macroscopic in the limit $T \to T_\mathrm{f}$. Above T_f wedge filling is continuous and is called complete wedge filling

by analogy with planar wetting [29, 46]. The apparent contact angle of approximately 45°, which one may infer from figures 8(a) and 8(c), illustrates that the filling of the wedge for $T_{\rm f} \leq T < T_{\rm w}$, proceeds via a continuously unbinding flat meniscus. The apparent contact angle should not be confused with Young's angle Θ, which is defined for a macroscopic sessile drop sitting on a flat planar wall at $\Delta\mu = 0$. In the case of the mesoscopic amount of liquid adsorbed in the wedge apex, both walls affect the fluid configuration, and a flat meniscus of zero curvature is energetically preferable to a curved one [46]. However, for a macroscopic amount of adsorbate at $T \geq T_{\rm f}$, the effect of one wedge wall on the contact line on the other becomes negligible and the apparent contact angle can attain values that are closer to $\Theta \leq \pi/4$ [46]. In contrast to the case of a non-zero Θ, for $T > T_{\rm w}$ the wetting films developing on the wedge walls lead to zero apparent contact angle of mesoscopic liquid adsorbate – see figure 8(b).

Computing $\mu_{\rm wpf}(T)$ (see figures 9 and 10) allows us to frame the discussion on phase transitions near the capping wall of the capillary in relation to its associated topologically-limiting systems. In very narrow pores, the effects of the Kelvin shift of bulk saturation are quite important, and lead to the wedge prefilling being pre-empted by capillary condensation, see, e.g. the wetting phase diagram in figure 5(a). Increasing H isolates the corners of the capped capillary, which may give rise to a metastable remnant wedge prefilling, $\tilde{\mu}_{\rm wpf}(T)$ (see figures 7 and 9, where $\mu_{\rm wpf}(T)$ and $\tilde{\mu}_{\rm wpf}(T)$ are plotted with dotted and solid curves, respectively). Note that in figure 9 the right-most end point of $\tilde{\mu}_{\rm wpf}(T)$ is a mean-field critical point, whereas the left-most end point corresponds to a situation where the branches of the grand potential which form the curve $\tilde{\mu}_{\rm wpf}(T)$ no longer intersect. Further increasing H significantly reduces the Kelvin shift while isolating the corners more. Eventually, the remnant wedge prefilling becomes stable, there may also be a triple point at $T^3_{\rm cpd}$, where gas, corner drops, and capillary liquid slab coexist (see the intersection of curves 6, 7 and 8 in figure 10). In the limit $H \to \infty$, $\tilde{\mu}_{\rm wpf}(T)$ tends to $\mu_{\rm wpf}(T)$, while at the same time $\mu_{\rm cpw}(T)$ tends to $\mu_{\rm pw}(T)$ of the capping wall. Since $T_{\rm f} < T_{\rm w}$, the triple point at $T^3_{\rm cpd}$ must disappear for large H. Therefore, stability of the three phases near the capping wall of the capillary is only possible for an intermediate range of mesoscopic capillary widths, and disappears in too narrow or too wide pores.

The phase diagram in figure 10 summarizes the mean-field wetting phenomenology of capped capillaries with mesoscopic values of H. The different transition curves and labels marking the regions of phase stability are coloured black for the structural transitions in the fluid associated with the capping wall (capillary prewetting, curves 6 and 8, and remnant wedge prefilling, curve 7), and grey for the transitions that also occur in the associated slit pore (condensation, curves 3 and 5, and remnant prewetting on the side walls, curve 4). Due to the Kelvin shift of bulk coexistence, remnant transitions in the capped capillary occur at lower values of the chemical potential than do wedge prefilling (curve 1) and planar prewetting (curve 2) [47], which are superimposed on the phase diagram to highlight the connections to these topologically limiting systems. Note that if considered on their own, the grey transition curves in figure 10 essentially

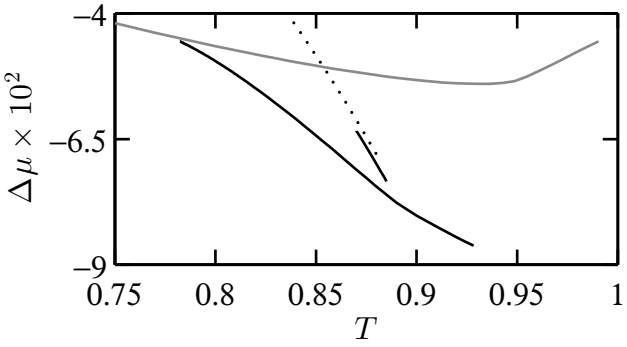

Figure 9. Wetting diagram of capped capillary with $H = 30$ and the same substrate as in figure 8 showing condensation (grey), wedge prefilling (black, $T_{\rm cw} = 0.780$), wedge prefilling (dotted) and its remnant in the capillary (black, which occurs approximately for $0.870 < T < 0.885$).

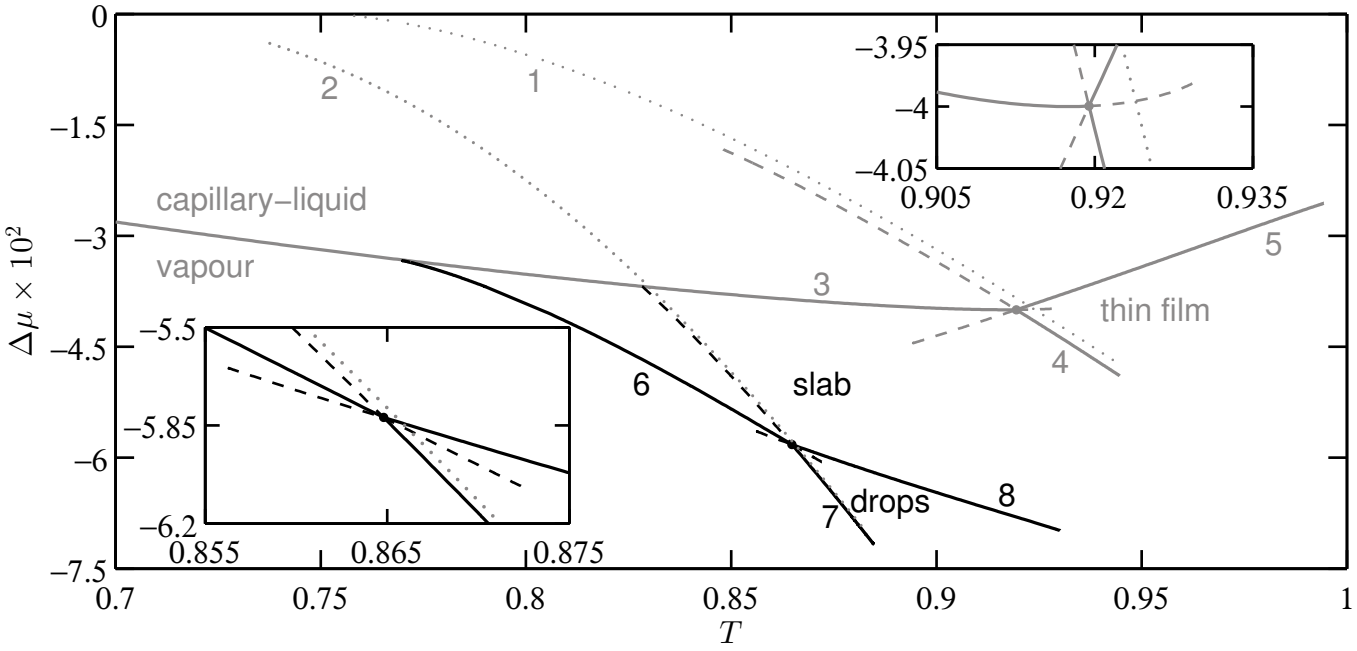

Figure 10. Wetting diagram of the capped capillary with $H = 40$; potential parameters are the same as in figure 8. Stable (solid) and metastable (dashed) transitions near the capping wall (black) and in the associated slit pore (grey) demarcate the regions of stability of different surface phases (labelled). Insets zoom into the triple points $T^3_{\rm cpd} = 0.865$ and $T^3_{\rm slt} = 0.920$. All transition curves are numbered. 1: planar prewetting ($T_{\rm w} = 0.755$); 2: wedge prefilling (only part shown, $T_{\rm f} = 0.693$); 3 and 5: condensation; 4: remnant of planar prewetting in the slit pore; 6 and 8: capillary prewetting ($T_{\rm cw} = 0.770$); 7: remnant of wedge prefilling in the capped capillary.

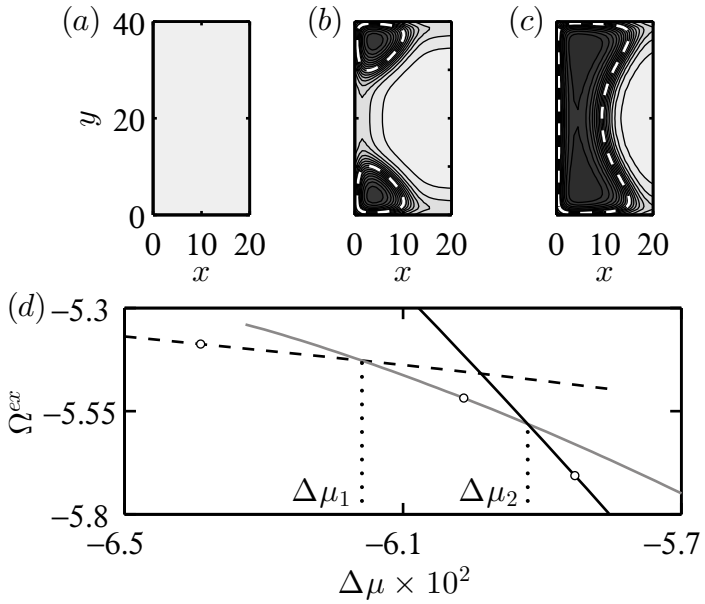

Figure 11. Three stable fluid surface phases in the capillary from figure 10 at $T = 0.87$ ($\rho^{\rm c}_{\rm vap} = 0.06$, $\rho^{\rm c}_{\rm liq} = 0.5$). (a)–(c) Representative density profiles of each phase. (d) Stable branches of the excess grand potential isotherm at $T = 0.87$: gas (dashed), drops (solid grey), and capillary liquid slab (solid black); $\Delta\mu_1 \equiv \Delta\mu_{\rm cpw}\,(T) = -6.15 \times 10^{-2}$, $\Delta\mu_2 \equiv \Delta\tilde{\mu}_{\rm wpf}\,(T) = -5.92 \times 10^{-2}$, $\Delta\mu_{\rm c} = -3.89 \times 10^{-2}$. Open circles correspond, from left to right, to the profiles in (a)–(c), respectively.

form the phase diagram of the associated slit pore. However, due to the interactions between the fluid and the capping wall, the first-order condensation of the slit pore and the first-order prewetting on the side walls of the slit pore become continuous transitions in the capped capillary. Our investigation of the continuous prewetting on the side walls is detailed in the following subsection.

Figure 11 shows the stable fluid phases just above $T^3_{\rm cpd}$. For $\Delta\mu < \Delta\mu_1 \equiv \Delta\mu_{\rm cpw}$ the pore is filled with gas – see figure 11(a). In the region $\Delta\mu_1 < \Delta\mu < \Delta\mu_2 \equiv \Delta\tilde{\mu}_{\rm wpf}$ corner drops – figure 11(b) – are stable and gas is metastable. For $\Delta\mu > \Delta\mu_2$ corner drops are metastable, and the liquid slabs – figure 11(c) – are stable. At $\Delta\mu_c$ the length of the liquid slab diverges. The $\Omega^{\rm ex}\,(\mu)$ isotherm – figure 11(d) – has three concave branches forming its lower envelope, and corresponding to each of the stable surface phases.

3.3. Prewetting on the side walls

For sufficiently large H there may be a remnant prewetting on the side walls of a slit pore at $\tilde{\mu}_{\rm pw} < \mu_{\rm c}$ [47]. Here we show how in capped capillaries with the same H, the capping wall may nucleate thick prewetting films below $\tilde{\mu}_{\rm pw}$. The wetting diagram in figure 10 provides an example of a capped capillary, where the associated slit pore has a triple point at $T^3_{\rm slt}$ (given by the intersection of curves 3, 4 and 5) corresponding to the coexistence between capillary vapor, capillary liquid and prewetting films. Fixing

$T = 0.93 \gtrsim T^3_{\rm slt}$, we computed an isotherm across the transition curves 8, 4 and 5. Representative density profiles in the capped capillary for μ below and above $\tilde{\mu}_{\rm pw}$ are presented in figures 12(a)–(c) and 12(d)–(f), respectively. We can see the interface between the thick and thin prewetting films unbind as μ approaches $\tilde{\mu}_{\rm pw}$ from below. Above $\tilde{\mu}_{\rm pw}$ the development of capillary liquid slab signifies continuous condensation. The corresponding isotherms of adsorption and excess grand potential in the capped capillary and in the associated slit pore at $T = 0.93$ are presented in figures 13(a)–(c). The filled and open circles on the isotherms correspond to the density profiles in figure 12, and are labelled accordingly in figure 13(a).

Consider first the excess grand potential of the associated slit pore $\Omega^{\rm ex}_{\rm slt}(\mu)$ given by

$$\Omega^{\rm ex}_{\rm slt}(\mu) = \Omega\left[\rho_{\rm slt}(y)\right] + AHP(\rho_{\rm b}), \tag{24}$$

where A is the surface area of the walls forming the slit pore and $\rho_{\rm b}$ is the bulk fluid density obtained from (16) [47]. Figure 13(c) shows the concave branches of $\Omega^{\rm ex}_{\rm slt}(\mu)$ corresponding to gas (dashed), prewetting films (solid grey) and capillary liquid (solid black). Remnant prewetting and condensation in the slit pore are first-order transitions which correspond to jump discontinuities in the lower envelope of $\Omega^{\rm ex}_{\rm slt}(\mu)$. Using the isotherm, we obtain $\Delta\mu_1$, $\Delta\mu_2 = \Delta\tilde{\mu}_{\rm pw}$ and $\Delta\mu_3 = \Delta\mu_{\rm c}$, which respectively correspond to the lower-μ spinodal of the remnant prewetting, remnant prewetting, and condensation. These values are marked by the labelled vertical dotted lines in figures 13(a)–(c).

Due to phase coexistence in the associated slit pore, there is an ambiguity in the definitions of $\Gamma(\tilde{\mu}_{\rm pw})$ and $\Omega^{\rm ex}(\tilde{\mu}_{\rm pw})$. In order to plot the branches of $\Gamma(\mu)$ and $\Omega^{\rm ex}(\mu)$ corresponding to prewetting (grey) and condensation (black) in figures 13(a) and 13(c), we used in (19) and (20) the density profiles of the coexisting thin and thick films, respectively. In the phase diagram in figure 10, the isotherm at $T = 0.93$ crosses transition curve 8 at $\Delta\mu_{\rm cpw} = -7 \times 10^{-2}$, and there is a corresponding near-critical hysteresis loop of $\Gamma(\mu)$ in figure 13(a).

The condensation branches of the wetting isotherms begin at $\Delta\mu_1$, but as can be inferred from figure 13(a), $\Gamma(\mu)$ decays between $\Delta\mu_1$ and $\Delta\mu_2$, so this part of the condensation branch is unstable (according to the Gibbs rule), and the system follows along the grey branch at $\Delta\mu_1 \leq \Delta\mu < \Delta\mu_2$. As $\Delta\mu \to \Delta\mu_2$ the thin-thick film interface unbinds from the capping wall at a rate which is controlled by the large-x asymptote of $V_{\rm cpd}(x, y)$, (18). Therefore, similarly to (21), the grey branch of $\Gamma(\mu)$ diverges as $\Gamma \propto (\mu - \tilde{\mu}_{\rm pw})^{-1/4}$ for $\mu \to \mu_{\rm pw} = \mu_2$. According to the Gibbs rule, the remnant prewetting is continuous in the capped capillary, since the derivative of the grand potential exhibits a singularity at $\Delta\mu_2$. For $\mu > \tilde{\mu}_{\rm pw}$, a capillary liquid slab is nucleated at the capping wall, and fills the capillary continuously as $\mu \to \mu_{\rm c} = \mu_3$. The adsorption and grand potential isotherms at $T > T^3_{\rm slt}$ (but not too far), thus, consist of two diverging branches, and there are two continuous transitions in the fluid – prewetting and condensation.

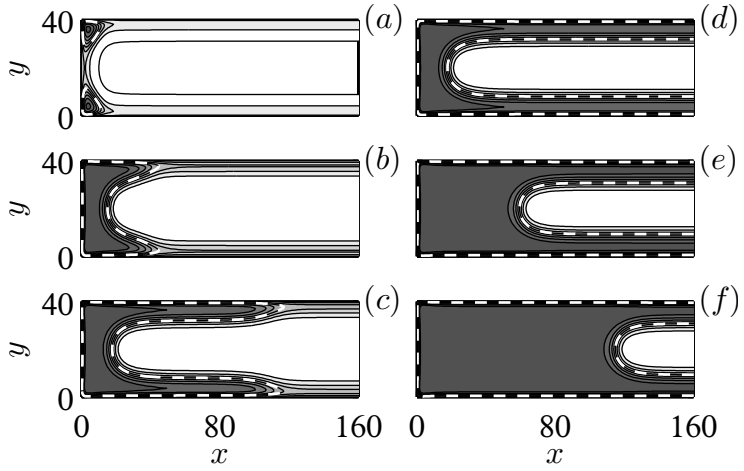

Figure 12. Density profiles at $T = 0.93$ ($\rho^{\rm c}_{\rm vap} = 0.09$, $\rho^{\rm c}_{\rm liq} = 0.41$) of the capped capillary from figure 10. (a)–(c) Approaching remnant prewetting from below, along the grey curve in figure 12(c); corresponding values of $\Delta\mu$ (top to bottom): $(-4.37; -3.82; -3.80) \times 10^{-2}$. (d)–(f) Above remnant prewetting, approaching condensation from below, along the black curve in figure 13(c); corresponding values of $\Delta\mu$ (top to bottom): $(-8.28; -4.62; -4.37) \times 10^{-2}$.

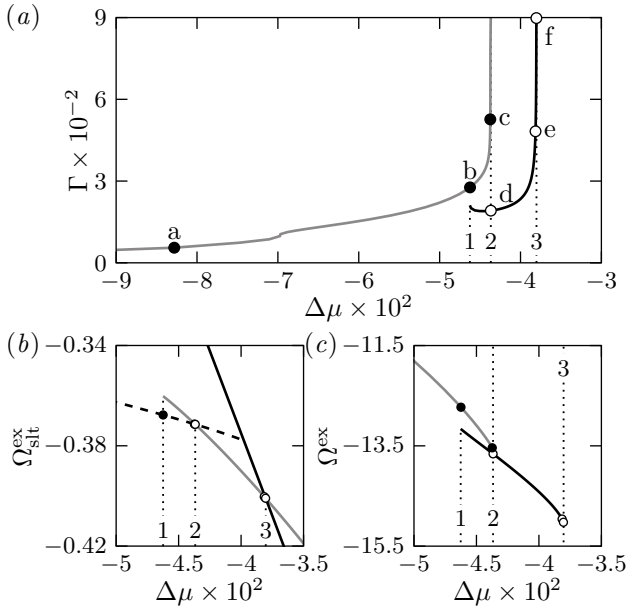

Figure 13. Isotherm at $T = 0.93$ in the capillary from figure 10; $\Delta\mu_1 = -4.6 \times 10^{-2}$, $\Delta\mu_2 \equiv \Delta\tilde{\mu}_{\rm pw}(T) = -4.37 \times 10^{-2}$, $\Delta\mu_3 \equiv \Delta\mu_{\rm c}(T) = -3.8 \times 10^{-2}$, marked by vertical dotted lines. (a) Adsorption isotherm of the capped capillary. Branches correspond to prewetting ($\mu < \mu_2$, grey) and condensation ($\mu_1 < \mu < \mu_3$, black). (b) Stable branches of the excess grand potential of the associated slit pore: gas (dashed), film (grey, spinodal at μ_1), and capillary liquid (black). (c) Excess grand potential of the capped capillary, branches colored as in (a). Filled and open circles correspond to profiles (a)–(c) and (d)–(f) in figure 12, respectively. Note that $\Gamma(\tilde{\mu}_{\rm pw})$ and $\Omega^{\rm ex}(\tilde{\mu}_{\rm pw})$ is defined differently for grey and black branches (see main text).

4. Conclusions

In this work we have investigated aspects of phase behavior of fluids confined to groove-like capillary pores of nanoscopic width. Computing the wetting phase diagrams of capped capillaries and their topologically limiting systems, i.e. planar walls, slit pores and wedges, allowed us to interpret various wetting mechanisms and capture the complexity of their fluid phase equilibria in groove-like pores. The investigation was based on DFTs with local and non-local hard sphere contributions, which are known to reproduce the qualitative aspects of wetting above the bulk triple point. We have considered a number of representative test cases in which a parametric study was undertaken by letting the temperature and chemical potential vary, while keeping all other parameters fixed. The results obtained are suggestive of the generic behavior of the system, and the methodology employed is applicable to similar studies of other pores. Since DFT retains microscopic details of the fluid at a significantly lower computational cost, compared to a molecular dynamics or Monte-Carlo simulations, the methodology developed for the purposes of the present study may provide an attractive tool for probing into the phase behavior of confined fluids.

Although capping a slit pore is a seemingly minor modification of its geometry, it leads to a strikingly different and rich physics of wetting. In particular, the order of condensation in a capped capillary depends on the applied temperature. It is first-order at $T \leq T_{\rm cw}$ and continuous at $T > T_{\rm cw}$, thus capillary wetting temperature $T_{\rm cw}$ is an important physical property of the system, which is determined by the microscopic details of fluid-fluid and fluid-substrate interactions. The fact that $T_{\rm cw}$ and $\mu_{\rm cpw}(T)$ exist in all of the capillaries considered and persist for both LDA and WDA for molecular fluid-fluid repulsions, suggests that the change of the order of condensation at $T_{\rm cw}$ and the existence of $\mu_{\rm cpw}(T)$ are generic features of the pore geometry. The width dependence of $T_{\rm cw}$ is investigated, e.g., in our previous work [25], where we have found that with increasing the pore width, $T_{\rm cw}$ tends to the planar wetting temperature $T_{\rm w}$ of the capping wall. Increasing the width of the pore isolates the corners and the side walls of the capped capillary, which lead to new physical effects. In particular, remnant wedge prefilling and remnant prewetting may be manifested by the adsorption of capillary liquid drops in the corners and films on the side walls of the capillary, respectively. The same effects can be brought about by choosing a substrate material with a lower wetting temperature. For example, the phase diagrams in figures 5(a) and 7 show how the remnant of wedge prefilling is brought into play by changing the fluid-substrate potential, and the phase diagrams in figures 9 and 10 show how the same effect occurs due to changes in the pore width.

The classical DFT has shown a possibility of the triple point at $T^3_{\rm cpd}$ between gas, corner drops and capillary liquid slab. Although, various fluctuation effects are omitted within DFT, there still may exist regimes where the structural transitions in the fluid near the capping wall can be experimentally accessible [29, 48]. On the other hand, the triple point at $T^3_{\rm slt}$ manifested by the coexistence between capillary vapor, liquid and

prewetting films, is known to exist beyond the classical picture [30]. As we have seen, for $T > T^3_{\rm slt}$ prewetting on the side walls takes place in continuous fashion. The prewetting films are nucleated at the capping wall below $\tilde{\mu}_{\rm pw}$, and grow with μ tending to $\tilde{\mu}_{\rm pw}$, so that in the limit $\mu \to \tilde{\mu}_{\rm pw}$, there are stable thick prewetting films covering the side walls of the capped capillary. Such behavior is demonstrative that prewetting on an isolated wall and on a side wall of a capillary may have different orders. We believe the continuous prewetting regime to be potentially important for experimental investigations of prewetting, since, as far as we are aware, registering experimentally the existence of the prewetting curve is notoriously difficult, as it spans a short range of temperatures and also lies very close to bulk saturation [30]. As a result, using capped pores may provide new possibilities and ideas to facilitate the design of intelligent experiments to capture prewetting. Noteworthy also is that this possibility to observe wall prewetting has been discussed, but not demonstrated as done here for capped capillaries, by Hauge for 2D wedges [46] and by Saam for step-like substrates [19].

As already mentioned, our present study neglects the fluctuations of the fluid density along the z-axis, because such an investigation requires a non-classical approach such as, e.g., that used in [24], and is beyond what DFT can offer at the moment. The capillary wave-like fluctuations of the interfaces along the z-axis are likely to affect the transitions discussed here, especially near their respective critical points. Investigations of criticality are certainly of interest and can form dedicated studies complementary to the present one [24, 29, 48]. Other studies expanding the present investigation may include wetting of non-homogeneous capped capillaries with corrugated or chemically decorated walls, investigation of layering transitions on the side walls, which may occur continuously, similarly to prewetting. The ramifications of multiple fluid phase equilibria for lowering the nucleation barriers and various other dynamic processes are also of interest, and may be investigated using dynamic DFT models, such as, e.g., those developed by Goddard *et al.* [18, 49].

Acknowledgments

We acknowledge financial support from the European Research Council via Advanced Grant No. 247031 and the European Union-FP7 ITN Grant No. 214919 (Multiflow). We are grateful to the anonymous referees for insightful comments and valuable suggestions and also to Professor Bob Evans and Professor Andy Parry for numerous stimulating discussions, insightful comments and constructive criticisms.

Appendix A. Interaction potentials and working expressions

Here we provide the expressions for the interaction potentials, which were used in computations. In all cases, the profile $\rho(\mathbf{r})$ is obtained by solving the Euler-Lagrange equation, (14). The non-local terms in (14) can be simplified considerably by integrating over the directions along which the density is assumed to be invariant. The expressions

that follow are based on the non-dimensionalization we have assumed throughout, setting $\sigma = 1$ and $\varepsilon = 1$.

In 1D problems the attractive term in (10) takes the form $\varphi_{\text{attr}}(y) \equiv \int \mathrm{d}z \int \mathrm{d}x \ \varphi_{\text{attr}}\left(\sqrt{x^2+y^2+z^2}\right)$:

$$\varphi_{\text{attr}}(y) = \begin{cases} -\dfrac{6\pi}{5}, & \text{if } |y| \leq 1, \\ 4\pi\left(\dfrac{1}{5y^{10}} - \dfrac{1}{2y^4}\right), & \text{if } |y| > 1. \end{cases} \tag{A.1}$$

The WDA weight-function in (13) takes the form:

$$W(y) = \frac{3}{4}\left(1-y^2\right)\Theta(1-y). \tag{A.2}$$

In 2D problems $\varphi_{\text{attr}}(x,y) \equiv \int \mathrm{d}z \ \varphi_{\text{attr}}\left(\sqrt{x^2+y^2+z^2}\right)$:

$$\varphi_{\text{attr}}(x,y) = \begin{cases} 2\displaystyle\int_{\sqrt{1-r^2}}^{\infty} \mathrm{d}z \ \varphi_{1,1}^{6-12}\left(\sqrt{r^2+z^2}\right), & \text{if } r \leq 1, \\ \dfrac{3\pi}{2}\left[-\left(\dfrac{1}{r}\right)^5 + \dfrac{21}{32}\left(\dfrac{1}{r}\right)^{11}\right], & \text{if } r > 1, \end{cases} \tag{A.3}$$

where $r = \sqrt{x^2+y^2}$. Although the integral in the above expression can be given in closed form for $r \leq 1$, see, e.g., the appendix in the study by Pereira and Kalliadasis [50], it is cumbersome and leads to roundoff errors and for these reasons it is computed numerically. When $r > 1$, we use the exact expression provided. The WDA weight-function in 2D problems is given by

$$W(x,y) = \frac{3\pi}{2}\left(1-r^2\right)\Theta(1-r). \tag{A.4}$$

All integrals in (4)–(7) can be obtained in closed form. In order to do so, we first found the potential V_0, due to a substrate occupying the space $\{(x,y,z) : x \leq 0, y \leq 0, -\infty < z < \infty$, namely:

$$V_0(x,y) = \rho_0 \int_{-\infty}^{\infty} \mathrm{d}z' \int_{-\infty}^{0} \mathrm{d}y' \int_{-\infty}^{0} \mathrm{d}x' \times \varphi_{\epsilon_0,\sigma_0}^{\text{LJ}}\left(\sqrt{(x-x')^2+(y-y')^2+z'^2}\right). \tag{A.5}$$

Computing the integrals yields

$$\begin{aligned} V_0(x,y) = {} & \frac{\rho_0\varepsilon_0\sigma_0^6\pi}{3}\left(-\frac{1}{x^3} - \frac{1}{y^3} + \frac{2x^4+x^2y^2+2y^4}{2x^3y^3\left(x^2+y^2\right)^{1/2}}\right) \\ & + \frac{2\rho_0\varepsilon_0\sigma_0^{12}\pi}{45}\left\{\frac{1}{x^9} + \frac{1}{y^9}\right. \\ & - \frac{1}{128x^9y^9\left(x^2+y^2\right)^{7/2}}\left[280\left(x^{10}y^6 + x^6y^{10}\right)\right. \end{aligned}$$

$$+128\left(x^{16}+y^{16}\right)+35x^8y^8+560\left(x^4y^{12}+x^{12}y^4\right)$$
$$+448\left(x^{14}y^2+x^2y^{14}\right)\big]\big\}\,, \tag{A.6}$$

so the substrate potentials are written as

$$V_{\mathrm{wll}}(x)=V_0(x+H_0,-y)+V_0(x+H_0,y)\,, \tag{A.7}$$

$$V_{\mathrm{wdg}}(x,y)=V_{\mathrm{wll}}(x)+V_0(-x-H_0,y)\,, \tag{A.8}$$

$$\begin{aligned}V_{\mathrm{cpd}}(x,y) &= V_{\mathrm{slt}}(x)+V_{\mathrm{wll}}(y)-V_0(x+H_0,y+H_0)\\ &\quad -V_0(-x-H_0-H,y+H_0)\,.\end{aligned} \tag{A.9}$$

Note that it readily follows from (A.6) and (A.7), that the coated planar wall has a well-known shifted "3-9" potential [33]:

$$V_{\mathrm{wll}}(x)=4\pi\rho_0\varepsilon_0\sigma_0^3\left(-\frac{1}{6}\left(\frac{\sigma_0}{H_0+x}\right)^3+\frac{1}{45}\left(\frac{\sigma_0}{H_0+x}\right)^9\right). \tag{A.10}$$

Appendix B. Convergence test

Here we present the test performed to assess the rate of convergence of the solutions to (14). Similar convergence tests for 1D and 2D problems can be found in our previous works, [25, 31]. For LDA, we considered a pore with $H=30\sigma$, $\varepsilon_0=0.7\varepsilon$, $\sigma_0=2\sigma$ and $H_0=5\sigma$, at $T=0.9$ and $\Delta\mu=-8\times10^{-2}$, where $\Delta\mu=\mu-\mu_{\mathrm{sat}}$ is under-saturation at the given T. For WDA, we considered a pore with $H=30\sigma$, $\varepsilon_0=0.85\varepsilon$, $\sigma_0=1.35\sigma$ and $H_0=2.2\sigma$, at $T=0.96$ and $\Delta\mu=-1.9\times10^{-2}$. With these parameters, we obtain density profiles which look similar to the density profile depicted in figure 2(a). The reference profile, denoted by ρ_0, was computed on a 162×80 grid along the x- and y-directions, respectively. The computation was repeated to obtain solutions ρ_N at coarser grids, where N is the total number of unknowns corresponding to the grids 32×16, 48×24, 72×36 and 108×54. In order to compare ρ_N with ρ_0, we interpolated both on a uniform grid of $K=40\times60$ points with the grid density of 2 points per molecular diameter along each dimension, and computed the mean Euclidean norm of the difference between the interpolated data:

$$\mathcal{E}=\frac{1}{K}\sqrt{\sum_{i=0}^{K}[\rho_N^{(i)}-\rho_0^{(i)}]^2}. \tag{B.1}$$

The results of this test are shown in figure B1, and demonstrate a satisfactory performance of the spectral collocation numerical scheme. Note that the calculation with WDA converges less rapidly due to the near-wall oscillatory structure of $\rho(\mathbf{r})$.

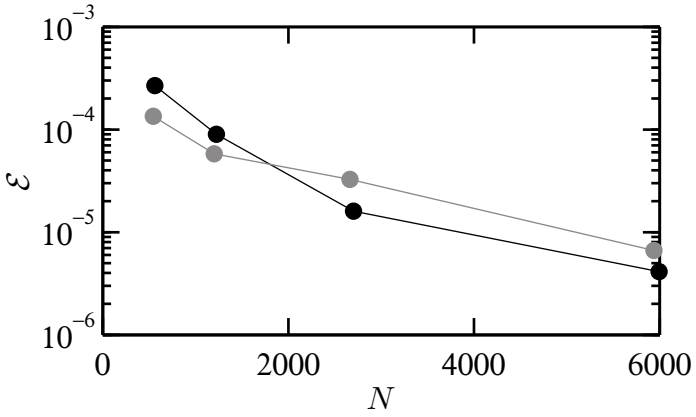

Figure B1. Convergence of solutions for 2D problems using LDA (grey) and WDA (black) with the number N of grid points. Circles represent convergence data.

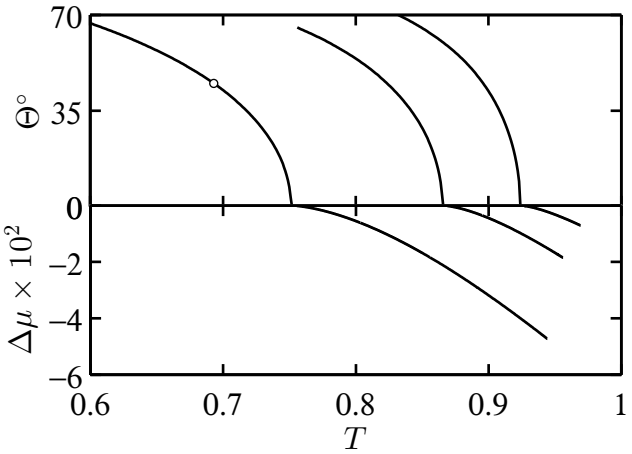

Figure C1. Young's contact angles (top panel) and planar wall prewetting curves (bottom panel) of the substrates considered. The respective substrate parameters $\{\varepsilon_0, \sigma_0, H_0\}$ are (left to right): {0.7, 2, 5} (LDA, $T_\mathrm{w} = 0.755$), {0.85, 1.5, 2.8} (WDA, $T_\mathrm{w} = 0.868$), {0.85, 1.35, 2.2} (WDA, $T_\mathrm{w} = 0.927$). The open circle shows the graphical solution of $\Theta(T_\mathrm{f}) = 45°$, which is used in section 3.2 to obtain the wedge filling temperature.

Appendix C. Planar wetting

Here we provide the planar prewetting curves, $\Delta\mu_\mathrm{pw}(T) = \mu_\mathrm{pw}(T) - \mu_\mathrm{sat}(T)$, and Young's contact angles, $\Theta(T)$, for the fluid-substrate potentials considered, which allow us to extract the values of T_w quoted throughout this work. The data is given in the system of units where $\varepsilon = 1$ and $\sigma = 1$ in (10). The computation was done by applying arc-length continuation in T to (15) with $V(\mathbf{r}) = V_\mathrm{wll}(y)$, as discussed in section 3.1, and detailed in our previous work [31]. We consider the following sets of substrate parameters $\{\varepsilon_0, \sigma_0, H_0\}$: for the fluid treated within WDA, we use {0.85, 1.35, 2.2} and {0.85, 1.5, 2.8}; for the fluid treated within LDA, we use {0.7, 2, 5}. The

computed $\Theta(T)$ and $\Delta\mu_{\rm pw}(T)$ curves for each set of parameters are plotted in the top and bottom panels of figure C1. As expected, the prewetting curves show a tangential approach to saturation ($\Delta\mu \equiv 0$) at $T_{\rm w}$ [19]. Young's contact angles vanish at the respective wetting temperatures, which further affirms the correct implementation of our numerics, because in practice $\Delta\mu_{\rm pw}(T)$ and $\Theta(T)$ are obtained independently from (15) and (14), respectively. Young's contact angle is defined by

$$\gamma_{\rm wv} - \gamma_{\rm wl} = \gamma_{\rm lv}\cos\Theta, \tag{C.1}$$

where $\gamma_{\rm wv}$ and $\gamma_{\rm wl}$ are the surface tensions of the saturated vapor and liquid in contact with the wall, respectively. The surface tension of a planar interface of area A is given by [45]

$$\gamma A = \Omega + PAL_{\perp}, \tag{C.2}$$

where Ω is the grand potential (8), P is the pressure (17), and $L_{\perp}$ is the dimension of the system in the direction perpendicular to the interface. The surface tensions $\gamma_{\rm wv}$ and $\gamma_{\rm wl}$ are obtained from (C.2) by setting $P = P_{\rm sat}$ of saturation in (17) and using the density profiles $\rho_{\rm vap}(y)$ and $\rho_{\rm liq}(y)$ of the saturated vapor and liquid in contact with the planar wall, with $\rho_{\rm vap}(y) \to \rho_{\rm vap}$ and $\rho_{\rm liq}(y) \to \rho_{\rm liq}$ as $y \to \infty$, respectively. The liquid-vapor surface tension $\gamma_{\rm lv}$ is obtained in the same manner, by setting $V(\mathbf{r}) \equiv 0$ in (14) and solving for the density profile $\rho_{\rm lv}(y)$ of the free liquid-vapor interface, taking $\rho_{\rm lv}(y) \to \rho_{\rm vap}$ and $\rho_{\rm lv}(y) \to \rho_{\rm liq}$ as $y \to \pm\infty$, respectively.

Appendix D. Slope of capillary prewetting

For fixed H, ε_0, σ_0 and H_0, the differential of the total energy of the fluid of N particles inside the capped capillary is given by

$$\mathrm{d}E = T\mathrm{d}S - P\mathrm{d}V + \mu\mathrm{d}N + \gamma\mathrm{d}A, \tag{D.1}$$

where S is the entropy, V is the fluid volume, γ is the interfacial tension and A is the surface area. With the Gibbs dividing surfaces defined for all interfaces, each extensive property can be expressed as the sum of volume and surface contributions, e.g., $N = \rho V + n_{\rm A}A$, where ρ and $n_{\rm A}$ are the number of particles per unit volume and per unit area, respectively. The Gibbs-Duhem relation, which follows from (D.1) has the form

$$S\mathrm{d}T - V\mathrm{d}P + N\mathrm{d}\mu + A\mathrm{d}\gamma = 0, \tag{D.2}$$

which leads to the Clausius-Clapeyron equation for the slope of a phase coexistence curve $\mu_{\rm coex}(T)$ in the T – μ plane:

$$\frac{\mathrm{d}\mu_{\rm coex}}{\mathrm{d}T} = -\frac{S_1 - S_2}{N_1 - N_2}, \tag{D.3}$$

where N_1, S_1 and N_2, S_2 are the particle numbers and entropies of the coexisting fluid phases. Equation (D.3) can be used, e.g., to relate the planar prewetting curve $\mu_{\rm pw}(T)$ to the saturation curve $\mu_{\rm sat}(T)$ [51–53]. Here we will use it to relate the prewetting curve

$\mu_{\rm cpw}(T)$ of the capped capillary to the condensation curve $\mu_{\rm c}(T)$ of the associated slit pore.

Consider a capillary with macroscopic dimensions L and R along the x- and z-axes, respectively. The number of particles, $N_1^{\rm cpd}$, in the fluid configuration, where a capillary liquid slab of length l is separated from gas by a meniscus is approximately written as

$$\begin{aligned} N_1^{\rm cpd} &= \rho_{\rm liq}^{\rm c} RHl + n_{\text{l-w}}^{\rm c} RH + 2n_{\text{l-w}}^{\rm c} Rl + n_{\text{l-g}}^{\rm c} A_{\text{l-g}} \\ &\quad + \rho_{\rm vap}^{\rm c} RH\,(L-l) + 2n_{\text{g-w}}^{\rm c} R\,(L-l)\,, \end{aligned} \tag{D.4}$$

where $n_{\text{l-w}}^{\rm c}$, $n_{\text{g-w}}^{\rm c}$ and $n_{\text{l-g}}^{\rm c}$ are the particle densities per area of the capillary liquid-wall, gas-wall, and capillary liquid-gas interfaces, respectively, and $A_{\text{l-g}}$ is the area of the capillary liquid-gas interface. Likewise, the number of particles $N_2^{\rm cpd}$ in the capillary filled by gas is found from

$$N_2^{\rm cpd} = \rho_{\rm vap}^{\rm c} RHL + n_{\text{g-w}}^{\rm c} RH + 2n_{\text{g-w}}^{\rm c} RL, \tag{D.5}$$

so that

$$\begin{aligned} N_1^{\rm cpd} - N_2^{\rm cpd} &= l\left[\rho_{\rm liq}^{\rm c} RH + 2n_{\text{l-w}}^{\rm c} R - \left(\rho_{\rm vap}^{\rm c} RH + 2n_{\text{g-w}}^{\rm c} R\right)\right] \\ &\quad + RH\left(n_{\text{l-w}}^{\rm c} - n_{\text{g-w}}^{\rm c}\right) + n_{\text{l-g}}^{\rm c} A_{\text{l-g}}. \end{aligned} \tag{D.6}$$

For the entropies $S_1^{\rm cpd}$ and $S_2^{\rm cpd}$, we use $S = \tilde{s}V + s_{\rm A}A$ to obtain a similar expression, where $\tilde{s}$ and $s_{\rm A}$ are the entropies per unit volume and per unit area of the interface, respectively

$$\begin{aligned} S_1^{\rm cpd} - S_2^{\rm cpd} &= l\left[\tilde{s}_{\rm liq}^{\rm c} RH + 2s_{\text{l-w}}^{\rm c} R - \left(\tilde{s}_{\rm vap}^{\rm c} RH + 2s_{\text{g-w}}^{\rm c} R\right)\right] \\ &\quad + RH\left(s_{\text{l-w}}^{\rm c} - s_{\text{g-w}}^{\rm c}\right) + s_{\text{l-g}}^{\rm c} A_{\text{l-g}}. \end{aligned} \tag{D.7}$$

Analogous considerations of the condensation in the associated slit pore lead to

$$N_1^{\rm slt} - N_2^{\rm slt} = L\left[\rho_{\rm liq}^{\rm c} RH + 2n_{\text{l-w}}^{\rm c} R - \left(\rho_{\rm vap}^{\rm c} RH + 2n_{\text{g-w}}^{\rm c} R\right)\right] \tag{D.8}$$

$$S_1^{\rm slt} - S_2^{\rm slt} = L\left[\tilde{s}_{\rm liq}^{\rm c} RH + 2s_{\text{l-w}}^{\rm c} R - \left(\tilde{s}_{\rm vap}^{\rm c} RH + 2s_{\text{g-w}}^{\rm c} R\right)\right], \tag{D.9}$$

where the phases 1 and 2 correspond to the pore filled with capillary liquid and gas, respectively. Substituting (D.6) and (D.7) into (D.3) with $N_{1,2} \equiv N_{1,2}^{\rm cpd}$, $S_{1,2} \equiv S_{1,2}^{\rm cpd}$ and $\mu_{\rm coex} \equiv \mu_{\rm cpd}$, we take the limit $l \to \infty$ and obtain

$$\frac{{\rm d}\mu_{\rm cpw}}{{\rm d}T} \to \frac{{\rm d}\mu_{\rm c}}{{\rm d}T}, \text{ as } l \to \infty. \tag{D.10}$$

The equation above demonstrates that $\mu_{\rm cpw}(T)$ approaches $\mu_{\rm c}(T)$ tangentially, as the length l of the coexisting capillary liquid slab grows. Furthermore, to leading order in l the difference $({\rm d}\mu_{\rm c}/{\rm d}T) - ({\rm d}\mu_{\rm cpw}/{\rm d}T)$ is inversely proportional to the first term on the right hand side of (D.6). Noting that for the spatially varying fluid density this term is given by the expression for Γ in (19) and that $l \to \infty$ is equivalent to $\Gamma \to \infty$, we arrive at (22).

References

[1] Rauscher M and Dietrich S 2008 *Annu. Rev. Mater. Res.* **38** 143

[2] Herminghaus S, Brinkman M and Seeman R 2008 *Annu. Rev. Mater. Res.* **38** 101
[3] Binder K 2008 *Annu. Rev. Mater. Res.* **38** 123
[4] Nosonvsky M and Bhushan B 2009 *Curr. Opin. Colloid. In.* **14** 270
[5] Craighead H 2006 *Nature* **442** 387
[6] Gou Z and Liu W 2007 *Plant Sci.* **172** 1103
[7] Calvo A, Yameen B, Williams F J, Soler-Illia G J A A and Azzaroni O 2009 *J. Am. Chem. Soc.* **131** 10866
[8] Lipowsky R 1984 *Phys. Rev. Lett.* **52** 1429
[9] Seeman R, Brinkman M, Kramer E J, Lange F F and Lipowsky R 2005 *Proc. Natl. Acad. Sci. U. S. A.* **102** 1848
[10] Gang O, Alvine K J, Fukuto M, Pershan P S, Black C T and Ocko B M 2005 *Phys. Rev. Lett.* **95** 217801
[11] Hamraoui A and Privat M 2009 *Adv. Colloid Interfac.* **149** 1–18
[12] Wu J 2006 *AIChE J.* **52** 1169
[13] Hansen J and McDonald I 2006 *Theory of Simple Liquids (3rd edn)* (Elsevier)
[14] Plischke M and Bergersen B 2006 *Equilibrium Statisitcal Physics* (World Scientific)
[15] Heffelfinger G S, Tan Z, Gubbins K E, Marconi U M B and Swol F v 1989 *Mol. Simulat.* **2** 393–411
[16] Lutsko J F 2010 Recent Developments in Classical Density Functional Theory *Adv. Chem. Phys.* (John Wiley & Sons) p 1
[17] Goddard B, Nold A, Savva N, Yatsyshin P and Kalliadasis S 2013 *J. Phys.: Condens. Matter* **25** 035101
[18] Goddard B, Nold A, Savva N, Pavliotis G A and Kalliadasis S 2012 *Phys. Rev. Lett.* **109** 120603
[19] Saam W F 2009 *J. Low Temp. Phys.* **157** 77
[20] Dietrich S 1988 Wetting Phenomena *Phase Transitions and Critical Phenomena* vol 12 ed Domb C and Lebowitz J L (Academic Press) p 2
[21] Bonn D and Ross D 2001 *Rep. Prog. Phys.* **64** 1085
[22] Parry A O, Rascon C, Wilding N B and Evans R 2007 *Phys. Rev. Lett.* **98** 226101
[23] Yatsyshin P, Savva N and Kalliadasis S 2013 *Phys. Rev. E* **87** 020402(R)
[24] Rascon C, Parry A, Nurnberg R, Pozzato A, Tormen M, Bruschi L and Mistura G 2013 *J. Phys. Condens. Matter* **25** 192101
[25] Yatsyshin P, Savva N and Kalliadasis S 2015 *J. Chem. Phys.* **142** 034708
[26] Darbellay G A and Yeomans J M 1992 *J. Phys. A-Math. Gen.* **25** 4275
[27] Roth R and Parry A O 2011 *Mol. Phys.* **109** 1159
[28] Malijevsky A 2012 *J. Chem. Phys.* **137** 214704
[29] Rejmer K, Dietrich S and Napiorkowski M 1999 *Phys. Rev. E* **60** 4027
[30] Evans R and Parry A 1990 *J. Phys. Condens. Matter* **2** SA 15
[31] Yatsyshin P, Savva N and Kalliadasis S 2012 *J. Chem. Phys.* **136** 124113
[32] Chizmeshya A, Cole M W and Zaremba Z 1998 *J. Low Temp. Phys.* **110** 677
[33] Sullivan D E and Telo da Gama M M 1986 Wetting Transitions and Multilayer Adsorption at Fluid Interfaces *Fluid Interfacial Phenomena* ed Croxton C A (Wiley, New York) p 45
[34] Zeng M, Mi J and Zhong C 2010 *Phys. Rev. B* **82** 125452
[35] Yu Y, Li Y and Zheng Y 2010 *Chin. Phys. Lett.* **27** 037101
[36] Sartarelli S A and Szybisz L 2009 *Phys. Rev. E* **80** 052602
[37] Ancilotto F and Toigo F 2000 *J. Chem. Phys.* **112** 4768
[38] Evans R 1990 Microscopic Theories of Simple Fluids and Their Interfaces *Les Houches 1988. Liquids at Interfaces.* ed Charvolin J, Joanny J F and Zinn-Justin J (North-Holland) p 1
[39] Barker J A and Henderson D 1967 *J. Chem. Phys.* **47** 4714
[40] Carnahan N F and Starling K E 1969 *J. Chem. Phys.* **51** 635
[41] Tarazona P and Evans R 1984 *Mol. Phys.* **52** 847
[42] Tarazona P, Cuesta J A and Martinez-Raton Y 2008 Density Functional Theories of Hard Particle Systems *Theory and Simulations of Hard-Sphere Fluids and Related Systems. Lecture Notes in*

Physics 753 ed Mulero A (Springer, Berlin Heidelberg) p 251
[43] Roth R 2010 *J. Phys.: Condens. Matter* **22** 063102
[44] Callen H B 1985 *Thermodynamics and an Introduction to Thermostatistics* (John Wiley & Sons, Inc.)
[45] Schick M 1990 Introduction to Wetting Phenomena *Les Houches 1988. Liquids at Interfaces.* ed Charvolin J, Joanny J F and Zinn-Justin J (North-Holland) p 415
[46] Hauge E H 1992 *Phys. Rev. A* **46** 4994
[47] Evans R and Marconi U M B 1987 *J. Chem. Phys.* **86** 7138
[48] Bieker T and Dietrich S 1998 *Physica A* **252** 85
[49] Goddard B, Nold A and Kalliadasis S 2013 *J. Chem. Phys.* **138** 144904
[50] Pereira A and Kalliadasis S 2012 *J. Fluid Mech.* **692** 53
[51] Hauge E H and Schick M 1983 *Phys. Rev. B* **27** 4288
[52] Saam W F, Treiner J, Cheng E and Cole M W 1992 *J. Low Temp. Phys.* **89** 637
[53] Cheng E, Mistura G, Lee H C, Chan M H W, Cole M W, Carraro C, Saam W F and Toigo F 1993 *Phys. Rev. Lett.* **70** 1854